

Inter-annual variability of the global terrestrial water cycle

Dongqin Yin^{1,2}, Michael L. Roderick^{1,3}

¹Research School of Earth Sciences, Australian National University, Canberra, ACT, 2601, Australia

²Australian Research Council Centre of Excellence for Climate System Science, Canberra, ACT, 2601, Australia

³Australian Research Council Centre of Excellence for Climate Extremes, Canberra, ACT, 2601, Australia

Correspondence to: (dongqin.yin@anu.edu.au & dongqin.yin@cau.edu.cn)

Abstract:

1 Variability of the terrestrial water cycle, i.e., precipitation (P), evapotranspiration (E), runoff (Q) and water
2 storage change (ΔS) is the key to understanding hydro-climate extremes. However, a comprehensive global
3 assessment for the partitioning of variability in P between E , Q and ΔS is still not available. In this study, we use
4 the recently released global monthly hydrologic reanalysis product known as the Climate Data Record (CDR) to
5 conduct an initial investigation of the inter-annual variability of the global terrestrial water cycle. We first
6 examine global patterns in partitioning the long-term mean \bar{P} between the various sinks \bar{E} , \bar{Q} and $\bar{\Delta S}$ and
7 confirm the well-known patterns with \bar{P} partitioned between \bar{E} and \bar{Q} according to the aridity index. In a new
8 analysis based on the concept of variability source and sinks we then examine how variability in the
9 precipitation σ_P^2 (the source) is partitioned between the three variability sinks σ_E^2 , σ_Q^2 and $\sigma_{\Delta S}^2$ along with the
10 three relevant covariance terms, and how that partitioning varies with the aridity index. We find that the
11 partitioning of inter-annual variability does not simply follow the mean state partitioning. Instead we find that
12 σ_P^2 is mostly partitioned between σ_Q^2 , $\sigma_{\Delta S}^2$ and the associated covariances with limited partitioning to σ_E^2 . We also
13 find that the magnitude of the covariance components can be large and often negative, indicating that variability
14 in the sinks (e.g., σ_Q^2 , $\sigma_{\Delta S}^2$) can, and regularly does, exceed variability in the source (σ_P^2). Further investigations
15 under extreme conditions revealed that in extremely dry environments the variance partitioning is closely related
16 to the water storage capacity. With limited storage capacity the partitioning of σ_P^2 is mostly to σ_E^2 , but as the
17 storage capacity increases the partitioning of σ_P^2 is increasingly shared between σ_E^2 , $\sigma_{\Delta S}^2$ and the covariance
18 between those variables. In other environments (i.e., extremely wet and semi-arid/semi-humid) the variance
19 partitioning proved to be extremely complex and a synthesis has not been developed. We anticipate that a major
20 scientific effort will be needed to develop a synthesis of hydrologic variability.

21 1. Introduction

22

23 In describing the terrestrial branch of the water cycle, the precipitation (P) is partitioned into evapotranspiration
24 (E), runoff (Q) and change in water storage (ΔS). With averages taken over many years, $\overline{\Delta S}$ is usually assumed to
25 be zero and it has long been recognized that the partitioning of the long-term mean annual precipitation (\overline{P})
26 between \overline{E} and \overline{Q} was jointly determined by the availability of both water (\overline{P}) and energy (represented by the net
27 radiation expressed as an equivalent depth of water and denoted $\overline{E_o}$). Using data from a large number of
28 watersheds, Budyko (1974) developed an empirical relation relating the evapotranspiration ratio ($\overline{E}/\overline{P}$) to the
29 aridity index ($\overline{E_o}/\overline{P}$). The resultant empirical relation and other Budyko-type forms (e.g., Fu, 1981; Choudhury,
30 1999; Yang et al., 2008, Roderick and Farquhar, 2011; Sposito, 2017) that partition P between E and Q have
31 proven to be extremely useful in both understanding and characterising the long-term mean annual hydrological
32 conditions in a given region.

33

34 However, the long-term mean annual hydrologic fluxes rarely occur in any given year. Instead, society must
35 (routinely) deal with variability around the long-term mean. The classic hydro-climate extremes are droughts and
36 floods but the key point here is that hydrologic variability is expressed on a full spectrum of time and space scales.
37 To accommodate that perspective, we need to extend our thinking beyond the long-term mean to ask how the
38 variability of P is partitioned into the variability of E , Q and ΔS (e.g., Orth and Destouni, 2018).

39

40 Early research on hydrologic variability focussed on extending the Budyko curve. In particular, Koster and Suarez
41 (1999) used the Budyko curve to investigate inter-annual variability in the water cycle. In their framework, the
42 evapotranspiration standard deviation ratio (defined as the ratio of standard deviation for E to P , σ_E/σ_P) was (also)
43 estimated using the aridity index ($\overline{E_o}/\overline{P}$). The classic Koster and Suarez framework has been widely applied and
44 extended in subsequent investigations of the variability in both E and Q , using catchment observations, reanalysis
45 data and model outputs (e.g., McMahon et al., 2011; Wang and Alimohammadi 2012; Sankarasubramanian and
46 Vogel, 2002; Zeng and Cai, 2015). However, typical applications of the Koster and Suarez framework have
47 previously been at regional scales and there is still no comprehensive global assessment for partitioning the
48 variability of P into the variability of E , Q and ΔS . One reason for the lack of a global comprehensive assessment
49 is the absence of gridded global hydrologic data. Interestingly, the atmospheric science community have long

50 used a combination of observations and model outputs to construct gridded global-scale atmospheric re-analyses
51 and such products have become central to atmospheric research. Those atmospheric products also contain
52 estimates of some of the key water cycle variables (e.g., P , E), such as in the widely used interim ECMWF Re-
53 Analysis (ERA-Interim; Dee et al. 2011). Though efforts have been taken to develop land-based products from
54 atmospheric reanalyses, e.g., ERA-Land (Balsamo et al., 2013) and MERRA-Land (Reichle et al., 2011) databases,
55 however, the central aim of atmospheric re-analysis is to estimate atmospheric variables. That atmospheric-centric
56 aim, understandably, ignores many of the nuances of soil water infiltration, vegetation water uptake, runoff
57 generation and many other processes of central importance in hydrology.

58

59 Hydrologists have only recently accepted the challenge of developing their own re-analysis type products with
60 perhaps the first serious hydrologic re-analysis being published as recently as a few years ago (Rodell et al., 2015).
61 More recently, the Princeton University group has extended this early work by making available a gridded global
62 terrestrial hydrologic re-analysis product known as the Climate Data Record (CDR) (Zhang et al., 2018). Briefly,
63 the CDR was constructed by synthesizing multiple in-situ observations, satellite remote sensing products, and
64 land surface model outputs to provide *gridded* estimates of global land precipitation P , evapotranspiration E ,
65 runoff Q and total water storage change ΔS ($0.5^\circ \times 0.5^\circ$, monthly, 1984-2010). In developing the CDR, the authors
66 adopted local water budget closure as the fundamental hydrologic principle. That approach presented one
67 important difficulty. Global observations of ΔS start with the GRACE satellite mission from 2002. Hence before
68 2002 there is no direct observational constraint on ΔS and the authors made the further assumption that the mean
69 annual ΔS over the full 1984-2010 period was zero at every grid-box. That is incorrect in some regions (e.g.
70 Scanlon et al., 2018) and represents an observational problem that cannot be overcome. However, our interest is
71 in the year-to-year variability and for that application, the assumption of no change in the mean annual ΔS over
72 the full 1984-2010 period is unlikely to lead to major problems since we are not looking for subtle changes over
73 time. With that caveat in mind, the aim of this study is to use this new 27-year gridded hydrologic re-analysis
74 product to conduct an initial investigation of the inter-annual variability of the terrestrial branch of the global
75 water cycle.

76

77 The paper is structured as follows. We begin in Section 2 by describing the various climate and hydrologic
78 databases used in this study, and also include a further assessment of the suitability of the CDR database for this

79 initial variability study. In Section 3, we examine relationships between the mean and variability in the four water
80 cycle variables (P , E , Q and ΔS). In Section 4, we first relate the variabilities to the classical aridity index and
81 then use those results to evaluate the theory of Koster and Suarez (1999). Subsequently we examine how the
82 variance of P is partitioned into the variances (and relevant covariances) of E , Q and ΔS and undertake an initial
83 survey that investigates some of the factors controlling the variance partitioning. We conclude the paper with a
84 discussion summarising what we have learnt about water cycle variability over land by using the CDR database.

85

86 2. Methods and Data

87 2.1 Methods

88 The water balance is defined by,

$$89 \quad P(t) = E(t) + Q(t) + \Delta S(t) \quad (1)$$

90 with P the precipitation, E the evapotranspiration, Q the runoff and ΔS the total water storage change in time
91 step t (annual in this study). By the usual variance law, we have,

$$92 \quad \sigma_P^2 = \sigma_E^2 + \sigma_Q^2 + \sigma_{\Delta S}^2 + 2cov(E, Q) + 2cov(E, \Delta S) + 2cov(Q, \Delta S) \quad (2)$$

93 that includes all relevant variances (denoted σ^2) and covariances (denoted cov). Eq. (2) can be thought of as the
94 hydrologic variance balance equation.

95

96 2.2 Hydrologic and Climatic Data

97

98 We use the Climate Data Record (CDR) database (Zhang et al., 2018) which is a recently released global land
99 hydrologic re-analysis. This product includes global precipitation P , evapotranspiration E , runoff Q and water
100 storage change ΔS ($0.5^\circ \times 0.5^\circ$, monthly, 1984-2010). In this study we focus on the inter-annual variability and
101 the monthly water cycle variables (P , E , Q and ΔS) are aggregated to annual totals. The CDR does not report
102 additional radiation variables and we use the NASA/GEWEX Surface Radiation Budget (SRB) Release-3.0
103 (monthly, 1984-2007, $1^\circ \times 1^\circ$) database (Stackhouse et al., 2011) to calculate E_o (defined as the net radiation
104 expressed as an equivalent depth of liquid water, Budyko, 1974). We then calculate the aridity index ($\overline{E_o}/\overline{P}$) using
105 P from the CDR and E_o from the SRB databases (see Fig. S1a in the Supplementary Material).

106

107 In general, we anticipate two important factors, i.e., the water storage capacity and the presence of ice/snow at the
108 surface, which are most likely to have influence on the partitioning of hydrologic variability. For the storage, the
109 active range of the monthly water storage variation was used to approximate the water storage capacity (S_{\max}). In
110 more detail, the water storage $S(t)$ at each time step t (monthly here) was first calculated from the accumulation
111 of $\Delta S(t)$, i.e., $S(t) = S(t-1) + \Delta S(t)$ where we assumed zero storage at the beginning of the study period (i.e., $S(0)$
112 = 0). With the resulting time series available, S_{\max} was estimated as the difference between the maximum and
113 minimum $S(t)$ during the study period at each grid-box (see Fig. S1b in the Supplementary Material). The
114 estimated S_{\max} shows a large range from 0 to 1000 mm with the majority of values from 50 to 600 mm (Fig. S1b),
115 which generally agrees with global rooting depth estimates assuming that water occupies from 10 to 30% of the
116 soil volume at field capacity (Jackson et al., 1996; Wang-Erlandsson et al., 2016; Yang et al., 2016). To
117 characterise snow/ice cover, and to distinguish extremely hot and cold regions, we also make use of a gridded
118 global land air temperature dataset from the Climatic Research Unit (CRU TS4.01 database, monthly, 1901-2016,
119 $0.5^\circ \times 0.5^\circ$) (Harris et al., 2014). (see Fig. S1c in the Supplementary Material).

120

121 2.3 Spatial Mask to Define Study Extent

122

123 The CDR database provides an estimate of the uncertainty ($\pm 1\sigma$) for each of the hydrologic variables (P , E , Q ,
124 ΔS) in each month. We use those uncertainty estimates to identify and remove regions with high relative
125 uncertainty in the CDR data. The relative uncertainty is calculated as the ratio of root mean square of the
126 uncertainty ($\pm 1\sigma$) to the mean annual P , E and Q at each grid-box following the procedure used by Milly and
127 Dunne (2002a). Note that the long term mean ΔS is zero by construction in the CDR database, and for that reason
128 we did not use ΔS to calculate the relative uncertainty. Grid-boxes with a relative uncertainty (in P , E and Q) of
129 more than 10% are deemed to have high relative uncertainty (Milly and Dunne, 2002a) and were excluded from
130 the study extent. The excluded grid-boxes were mostly in the Himalayan region, the Sahara Desert and in
131 Greenland. The final spatial mask is shown in Fig. S2 and this has been applied throughout this study.

132

133 2.4 Further Evaluation of CDR Data for Variability Analysis

134

135 In the original work, the CDR database was validated by comparison with independent observations including (i)
136 mean seasonal cycle of Q from 26 large basins (see Fig. 8 in Zhang et al., 2018), (ii) mean seasonal cycle of ΔS

137 from 12 large basins (Fig. 10 in Zhang et al., 2018), (iii) monthly runoff from 165 medium size basins and a
138 further 862 small basins (Fig. 14 in Zhang et al., 2018), (iv) summer E from 47 flux towers (Fig. 16 in Zhang et
139 al., 2018). Those evaluations did not directly address variability in various water cycle elements. With our focus
140 on the variability we decided to conduct further validations of the CDR database beyond those described in the
141 original work. In particular, we focussed on further independent assessments of E and we use monthly (as opposed
142 to summer) observations of E from FLUXNET to evaluate the variability in E . We also compare the
143 evapotranspiration E in the CDR with two other gridded global E products that were not used to develop the CDR
144 including the LandFluxEval database ($1^\circ \times 1^\circ$, monthly, 1989-2005) (Mueller et al., 2013) and the Max Planck
145 Institute database (MPI, $0.5^\circ \times 0.5^\circ$, monthly, 1982-2011) (Jung et al., 2010). The runoff Q in the CDR is further
146 compared with the gridded European Q product E-RUN ($0.5^\circ \times 0.5^\circ$, monthly, 1951-2015) (Gudmundsson and
147 Seneviratne, 2016).

148

149 For the comparison to FLUXNET observations (Baldocchi et al., 2001; Agarwal et al., 2010) we identified 32
150 flux tower sites (site locations are shown in Fig. S3 and details are shown in Table S1) having at least three years
151 of continuous (monthly) measurements using the FluxnetLSM R package (v1.0) (Ukkola et al. 2017). The monthly
152 totals and annual climatology of P and E from CDR generally follow FLUXNET observations, with high
153 correlations and reasonable Root Mean Square Error (Figs. S4-S5, Table S1). Comparison of the point-based
154 FLUXNET (~ 100 m – 1 km scale) with the grid-based CDR (~ 50 km scale) is problematic since the CDR
155 represents an area that is at least 2500 times larger than the area represented by the individual FLUXNET towers
156 and we anticipate that the CDR record would be “smoothed” relative to the FLUXNET record. With that in mind,
157 we chose to compare the ratio of the standard deviation of E to P between the CDR and FLUXNET databases and
158 this normalised comparison of the hydrologic variability proved encouraging (Fig. S6).

159

160 The comparison of E between the CDR and the LandFluxEval and MPI databases also proved encouraging. We
161 found that the monthly mean E from the CDR database is slightly underestimated compared with LandFluxEval
162 database (Fig. S7a), but agrees closely with the MPI database (Fig. S8a). In terms of variability, the standard
163 deviations of monthly E from the CDR are in very close agreement with the LandFluxEval database (Fig. S7c),
164 but there is a bias and scaling offset for the comparison with the MPI database particularly for the grid-cells with
165 low standard deviation of E (Fig. S8c). The comparison of runoff Q between the E-RUN and CDR databases show
166 that the two databases have very similar spatial patterns of both the long-term mean (\bar{Q}) and standard deviation

167 (σ_Q) of the monthly Q (Fig. S10). The grid-by-grid comparison results are also encouraging, showing slight bias
168 of both the long-term mean and standard deviation of monthly Q in the CDR database compared with the E-RUN
169 database (Fig. S11).

170

171 We concluded that while the CDR database was unlikely to be perfect, it was nevertheless suitable for an initial
172 exploratory survey of inter-annual variability in the terrestrial branch of the global water cycle.

173

174 **3. Mean and Variability of Water Cycle Components**

175 3.1 Mean Annual P , E , Q and the Budyko Curve

176

177 The global pattern of mean annual P , E , Q using the CDR data (1984-2007) is shown in Fig. 1. The mean annual
178 P (\bar{P}) is prominent in tropical regions, southern China, eastern and western North America (Fig. 1a). The
179 magnitude of mean annual E (\bar{E}) more or less follows the pattern of \bar{P} in the tropics (Fig. 1b) while the mean
180 annual Q (\bar{Q}) is particularly prominent in the Amazon, South and Southeast Asia, tropical parts of west Africa
181 and in some other coastal regions at higher latitudes (Fig. 1c).

182

183 We relate the grid-box level ratio of \bar{E} to \bar{P} in the CDR database to the classical Budyko (1974) curve using the
184 aridity index (\bar{E}_o/\bar{P}) (Fig. 2a). As noted previously, in the CDR database, $\bar{\Delta S}$ is forced to be zero and this enforced
185 steady state (i.e., $\bar{P} = \bar{E} + \bar{Q}$) allowed us to also predict the ratio of \bar{Q} to \bar{P} using the same Budyko curve (Fig.
186 2b). The Budyko curves follow the overall pattern in the CDR data, which agrees with previous studies showing
187 that the aridity index can be used to predict water availability (e.g., Gudmundsson et al., 2016). However, there is
188 substantial scatter due to, for example, regional variations related to seasonality, water storage change and the
189 landscape characteristics (Milly, 1994a, b, Padrón et al., 2017). With that caveat in mind, the overall patterns are
190 as expected with \bar{E} following \bar{P} in dry environments ($\bar{E}_o/\bar{P} > 1.0$) while \bar{E} follows \bar{E}_o in wet environments
191 ($\bar{E}_o/\bar{P} \leq 1.0$) (Fig. 2).

192

193 3.2 Inter-annual Variability in P , E , Q and ΔS

194

195 We use the variance balance equation (Eq. 2) to partition the inter-annual σ_P^2 into separate components due to σ_E^2 ,
196 σ_Q^2 , $\sigma_{\Delta S}^2$ along with the three covariance components ($2cov(E, Q)$, $2cov(E, \Delta S)$, $2cov(Q, \Delta S)$) (Fig. 3). The

197 spatial pattern of σ_P^2 (Fig. 3a) is very similar to that of \bar{P} (Fig. 1a), which implies that the σ_P^2 is positively
198 correlated with \bar{P} . In contrast the partitioning of σ_P^2 to the various components is very different from the
199 partitioning of \bar{P} (cf. Fig. 1 and 3). First we note that while the overall spatial pattern of σ_E^2 more or less follows
200 σ_P^2 , the overall magnitude of σ_E^2 is much smaller than σ_P^2 and σ_Q^2 in most regions, and in fact σ_E^2 is also generally
201 smaller than $\sigma_{\Delta S}^2$. The prominence of $\sigma_{\Delta S}^2$ (compared to σ_E^2) surprised us. The three covariance components
202 ($cov(E, Q)$, $cov(E, \Delta S)$, $cov(Q, \Delta S)$) are also important in some regions. In more detail, the $cov(E, Q)$ term is
203 prominent in regions where σ_Q^2 is large and is mostly negative in those regions (Fig. 3e), indicating that years with
204 lower E are associated with higher Q and vice-versa. There are also a few regions with prominent positive values
205 for $cov(E, Q)$ (e.g., the seasonal hydroclimates of northern Australia) indicating that in those regions, years with
206 a higher E are associated with higher Q . The $cov(E, \Delta S)$ term (Fig. 3f) has a similar spatial pattern to the
207 $cov(E, Q)$ term (Fig. 3e) but with a smaller overall magnitude. Finally, the $cov(Q, \Delta S)$ term shows a more
208 complex spatial pattern, with both prominent positive and negative values (Fig. 3g) in regions where σ_Q^2 (Fig. 3c)
209 and $\sigma_{\Delta S}^2$ (Fig. 3d) are both large.

210

211 These results show that the spatial patterns in variability are not simply a reflection of patterns in the long-term
212 mean state. On the contrary, we find that of the three primary variance terms, the overall magnitude of (inter-
213 annual) σ_E^2 is the smallest implying the least (inter-annual) variability in E . This is very different from the
214 conclusions based on spatial patterns in the mean P , E and Q (see section 3.1). Further, while σ_Q^2 more or less
215 follows σ_P^2 as expected, we were surprised by the magnitude of $\sigma_{\Delta S}^2$ which, in general, substantially exceeds the
216 magnitude of σ_E^2 . Further, the magnitude of the covariance terms can be important, especially in regions with high
217 σ_Q^2 . However, unlike the variances, the covariance can be both positive and negative and this introduces additional
218 complexity. For example, with a negative covariance it is possible for the variance in Q (σ_Q^2) to exceed the variance
219 in P (σ_P^2). To examine that in more detail we calculated the equivalent frequency distribution for each of the plots
220 in Fig. 3. The results (Fig. S9) further emphasise that in general, σ_E^2 is the smallest of the variances (Fig. S9b).
221 We also note that the frequency distributions for the covariances (Fig. S9efg) are not symmetrical. In summary,
222 it is clear that spatial patterns in the inter-annual variability of the water cycle (Fig. 3) do not simply follow the
223 spatial patterns for the inter-annual mean (Fig. 1).

224

225 3.3 Relation Between Variability and the Mean State for P, E, Q

226

227 Differences in the spatial patterns of the mean (Fig. 1) and inter-annual variability (Fig. 3) in the global water
228 cycle led us to further investigate the relation between the mean and the variability for each separate component.
229 Here we relate the standard deviation ($\sigma_P, \sigma_E, \sigma_Q$) instead of the variance to the mean of each water balance flux
230 (Fig. 4) since the standard deviation has the same physical units as the mean making the results more comparable.
231 As inferred previously, we find σ_P to be positively correlated with \bar{P} but with substantial scatter (Fig. 4a). The
232 same result more or less holds for the relation between σ_Q and \bar{Q} (Fig. 4c). In contrast the relation between σ_E and
233 \bar{E} is very different (Fig. 4b). In particular, σ_E is a small fraction of \bar{E} and this complements the earlier finding (Fig.
234 4b) that the inter-annual variability for E is generally smaller than for the other physical variables (P, Q and ΔS).
235 (The same result was also found using both LandFluxEVAL and MPI databases, see Fig. S12 in the
236 Supplementary Material.) Importantly, unlike P and Q, E is constrained by both water and energy availability
237 (Budyko, 1974) and the limited inter-annual variability in E presumably reflects limited inter-annual variability
238 in the available (radiant) energy (E_o). This is something that could be investigated in a future study.

239

240 4. Relating the Variability of Water Cycle Components to Aridity

241 In the previous section, we investigated spatial patterns of the mean and the variability in the global water cycle.
242 In this section, we extend that by investigating the partitioning of σ_P^2 to the three primary physical terms ($\sigma_E^2, \sigma_Q^2,$
243 $\sigma_{\Delta S}^2$) along with the three relevant covariances. For that, we begin by comparing the Koster and Suarez (1999)
244 theory against the CDR data and then investigate how the partitioning of the variance is related to the aridity index
245 \bar{E}_o/\bar{P} (see Fig. S1a in the Supplementary Material). Following that, we investigate variance partitioning in relation
246 to both our estimate of the storage capacity S_{\max} (see Fig. S1b in the Supplementary Material) as well as the mean
247 annual air temperature \bar{T}_a (see Fig. S1c in the Supplementary Material) that we use as a surrogate for snow/ice
248 cover. We finalise this section by examining the partitioning of variance at three selected study sites that represent
249 extremely dry/wet, high/low water storage capacity and the hot/cold spectrums.

250

251 4.1 Comparison with the Koster and Suarez (1999) Theory

252

253 We first evaluate the classical empirical curve of Koster and Suarez (1999) by relating ratios σ_E/σ_P and σ_E/σ_P to
254 the aridity index (Fig. 5). The ratio σ_E/σ_P in the CDR database is generally overestimated by the empirical Koster

255 and Suarez curve, especially in dry environments (e.g., $\overline{E_o}/\overline{P} > 3$) (Fig. 5a). The inference here is that the Koster
256 and Suarez theory predicts σ_E/σ_P to approach unity in dry environments while the equivalent value in the CDR
257 data is occasionally unity but is generally smaller. With σ_E/σ_P generally overestimated by the Koster and Suarez
258 theory we expect, and find, that σ_Q/σ_P is generally underestimated by the same theory (Fig. 5b). The same
259 overestimation was found based on the other two independent databases for E (LandFluxEVAL and MPI) (Fig.
260 S13). This overestimation is discussed further in section 5.

261

262 4.2 Relating Inter-annual Variability to Aridity

263

264 Here we examine how the fraction of the total variance in precipitation accounted for by the three primary variance
265 terms along with the three covariance terms varies with the aridity index ($\overline{E_o}/\overline{P}$) (Fig. 6). (Also see Fig. S14 for
266 the spatial maps.) The ratio σ_E^2/σ_P^2 is close to zero in extremely wet regions and has an upper limit noted
267 previously (Fig. 5a) that approaches unity in extremely dry regions (Fig. 6a). The ratio σ_Q^2/σ_P^2 is close to zero in
268 extremely dry regions but approaches unity in extremely wet regions but with substantial scatter (Fig. 6b). The
269 ratio $\sigma_{\Delta S}^2/\sigma_P^2$ is close to zero in both extremely dry/wet regions (Fig. 6c) and shows the largest range at an
270 intermediate aridity index ($\overline{E_o}/\overline{P} \sim 1.0$).

271

272 The covariance ratios are all small in extremely dry (e.g., $\overline{E_o}/\overline{P} \geq 6.0$) environments and generally show the largest
273 range in semi-arid and semi-humid environments. The peak magnitudes for the three covariance components
274 consistently occur when $\overline{E_o}/\overline{P}$ is close to 1.0 which is the threshold often used to separate wet and dry
275 environments.

276

277 4.3 Further Investigations on the Factors Controlling Partitioning of the Variance

278

279 Results in the previous section demonstrated that spatial variation in the partitioning of σ_P^2 into σ_E^2 , σ_Q^2 , $\sigma_{\Delta S}^2$ and
280 the three covariance components is complex (Fig. 6). To help further understand inter-annual variability of the
281 terrestrial water cycle, we conduct further investigations in this section using two factors likely to have a major
282 influence on the variance partitioning of σ_P^2 . The first is the storage capacity S_{\max} (see Fig. S1b in the
283 Supplementary Material). The second is the mean annual air temperature $\overline{T_a}$ (see Fig. S1c in the Supplementary
284 Material) which is used here as a surrogate for snow/ice presence.

285

286 4.3.1 Relating Inter-annual Variability to Storage Capacity

287

288 We first relate the partitioning of σ_P^2 to water storage capacity (S_{\max}) by repeating Fig. 6 but instead we use a
289 logarithmic scale for the x-axis and we distinguish S_{\max} via the background colour (Fig. 7). To eliminate the
290 possible overlap of grid-cells in the colouring process, all the grid-cells over land are further separated using
291 different latitude ranges (as shown in the four columns of Fig. 7), i.e., 90N-60N, 60N-30N, 30N-0 and 0-90S. We
292 find that S_{\max} is relatively high in wet environments ($\overline{E_o}/\overline{P} \leq 1.0$, Fig. 7a) but shows no obvious relation to the
293 partitioning of σ_P^2 . However, in dry environments ($\overline{E_o}/\overline{P} > 1.0$) the ratio σ_E^2/σ_P^2 apparently decreases with the
294 increase of S_{\max} (Fig. 7a-d). That relation is particularly obvious in extremely dry environments ($\overline{E_o}/\overline{P} \geq 6.0$) at
295 equatorial latitudes where there is an upper limit of σ_E^2/σ_P^2 close to 1.0 when S_{\max} is small (blue grid-cells in Fig.
296 7c). The interpretation for those extremely dry environments is that when S_{\max} is small, σ_P^2 is almost completely
297 partitioned into σ_E^2 (Fig. 7bc) with the other variance and covariance components close to zero. While for those
298 same extremely dry environments, as S_{\max} increases, the partitioning of σ_P^2 is shared between σ_E^2 and $\sigma_{\Delta S}^2$ and their
299 covariance (Fig. 7cks) while σ_Q^2 and its covariance components remain close to zero (Fig. 7gow). However, at
300 polar latitudes in the northern hemisphere (panels in the first and second columns of Fig. 7) there are variations
301 that could not be easily associated with variations in S_{\max} which led us to further investigate the role of snow/ice
302 on the variance partitioning in the following section.

303

304 4.3.2 Relating Inter-annual Variability to Mean Air Temperature

305

306 To understand the potential role of snow/ice in modifying the variance partitioning, we repeat the previous
307 analysis (Fig. 7) but here we use the mean annual air temperature ($\overline{T_a}$) to colour the grid-cells to (crudely) indicate
308 the presence of snow/ice (Fig. 8). The results are complex and not easy to simply understand. The most important
309 difference revealed by this analysis is in the hydrologic partitioning between cold (first column) and hot (third
310 column) conditions in wet environments ($\overline{E_o}/\overline{P} \leq 0.5$). In particular, when $\overline{T_a}$ is high, σ_P^2 is almost completely
311 partitioned into σ_Q^2 in wet environments (e.g., $\overline{E_o}/\overline{P} \leq 0.5$, Fig. 8g). In contrast, when $\overline{T_a}$ is low in a wet
312 environment ($\overline{E_o}/\overline{P} \leq 0.5$ in first column of Fig. 8), there are substantial variations in the hydrologic partitioning.
313 That result reinforces the complexity of variance partitioning in the presence of snow/ice.

314

315 4.4 Case Studies

316

317 The previous results (Section 4.3) have demonstrated that the partitioning of σ_P^2 is influenced by the water storage
 318 capacity (S_{\max}) in extremely dry environments ($\overline{E_o}/\overline{P} \geq 6.0$) and that the presence of snow/ice is important (as
 319 indicated by mean air temperature ($\overline{T_a}$)) in extremely wet environments ($\overline{E_o}/\overline{P} \leq 0.5$). In this section, we examine,
 320 in greater detail, several sites to gain deeper understanding of the partitioning of σ_P^2 . For that purpose, we selected
 321 three sites based on extreme values for the three explanatory parameters, i.e., $\overline{E_o}/\overline{P}$ (Fig. S1a), S_{\max} (Fig. S1b) and
 322 $\overline{T_a}$ (Fig. S1c). The criteria to select three climate sites are as follows, Site 1: dry ($\overline{E_o}/\overline{P} \geq 6.0$) and small S_{\max} (S_{\max}
 323 ≈ 0), Site 2: dry ($\overline{E_o}/\overline{P} \geq 6.0$) and relatively large S_{\max} ($S_{\max} \gg 0$) and Site 3: wet ($\overline{E_o}/\overline{P} \leq 0.5$) and hot ($\overline{T_a} > 25$
 324 $^{\circ}\text{C}$). For each of the three classes, we use a representative grid-cell (Fig. 9) to show the original time series (Fig.
 325 10) and the partitioning of the variability (Fig. 11).

326

327 We show the P , E , Q and ΔS time series along with the relevant variances and covariances in Fig. 10. Starting
 328 with the two dry sites, at the site with low storage capacity (Site 1), the time series shows that E closely follows
 329 P leaving annual Q and ΔS close to zero (Fig. 10a). The variance of P ($\sigma_P^2 = 206.9 \text{ mm}^2$) is small and almost
 330 completely partitioned into the variance of E ($\sigma_E^2 = 196.9 \text{ mm}^2$), leaving very limited variance for Q , ΔS and all
 331 three covariance components (Fig. 10b). At the dry site with larger storage capacity (Site 2), E , Q and ΔS do not
 332 simply follow P (Fig. 10c). As a consequence, the variance of P ($\sigma_P^2 = 2798.0 \text{ mm}^2$) is shared between E ($\sigma_E^2 =$
 333 1150.2 mm^2), ΔS ($\sigma_{\Delta S}^2 = 800.5 \text{ mm}^2$) and their covariance component ($2cov(E, \Delta S) = 538.4 \text{ mm}^2$, Fig. 10d).
 334 Switching now to the remaining wet and hot site (Site 3), we note that Q closely follows P , with ΔS close to zero
 335 and E showing little inter-annual variation (Fig. 10e). The variance of P ($\sigma_P^2 = 57374.4 \text{ mm}^2$) is relatively large
 336 and almost completely partitioned into the variance of Q ($\sigma_Q^2 = 57296.4 \text{ mm}^2$), leaving very limited variance for
 337 E and ΔS and the three covariance components (Fig. 10f). We also examined numerous other sites with similar
 338 extreme conditions as the three case study sites and found the same basic patterns as reported above.

339

340 To put the data from the three case study sites into a broader variability context we position the site data onto a
 341 backdrop of original Fig. 6. As noted previously, at Site 1, the ratio σ_E^2/σ_P^2 is very close to unity (Fig. 11a), and
 342 under this extreme condition, we have the following approximation,

343
$$\sigma_P^2 \approx \sigma_E^2 \quad (\text{Site 1, dry and } S_{\max} \approx 0) \quad (3)$$

344 In contrast, for Site 2 with the same aridity index but higher S_{\max} , we have,

345
$$\sigma_P^2 \approx \sigma_E^2 + \sigma_{\Delta S}^2 + 2cov(E, \Delta S) \quad (\text{Site 2, dry and } S_{\max} \gg 0) \quad (4)$$

346 Finally, at Site 3, we have,

347
$$\sigma_P^2 \approx \sigma_Q^2 \quad (\text{Site 3, wet and hot}) \quad (5)$$

348

349 4.5 Synthesis

350

351 The above simple examples demonstrate that aridity $\overline{E_o}/\overline{P}$, storage capacity S_{\max} and to a lesser extent, air
 352 temperature $\overline{T_a}$, all play some role in the partitioning of σ_P^2 to the various components. Our synthesis of the results
 353 for the partitioning of σ_P^2 is summarised in Fig. 12. In dry environments with low storage capacity ($S_{\max} \approx 0$) we
 354 have minimal runoff and expect that σ_P^2 is more or less completely partitioned into σ_E^2 (Fig. 12a). In those
 355 environments, (inter-annual) variations in storage $\sigma_{\Delta S}^2$ play a limited role in setting the overall variability.
 356 However, in dry environments with larger storage capacity ($S_{\max} \gg 0$), σ_E^2 is only a small fraction of σ_P^2 (Fig. 12a)
 357 leaving most of the overall variance in σ_P^2 to be partitioned to $\sigma_{\Delta S}^2$ and the covariance between E and ΔS (Fig.
 358 12c and Fig. 12e). This emphasises the hydrological importance of water storage capacity in buffering variations
 359 of the water cycle under dry conditions.

360

361 Under extremely wet conditions, the largest difference in variance partitioning is not due to differences in storage
 362 capacity but is instead related to differences in mean air temperature. In wet and hot environments, we have
 363 maximum runoff and find that σ_P^2 is more or less completely partitioned into σ_Q^2 (Fig. 12b) while the partitioning
 364 to σ_E^2 and $\sigma_{\Delta S}^2$ is small. However, in wet and cold environments, the variance partitioning shows great complexity
 365 with σ_P^2 being partitioned into all possible components. We suggest that this emphasises the hydrological
 366 importance of thermal processes (melting/freezing) under extremely cold conditions.

367

368 However, the most complex patterns to interpret are those for semi-arid to semi-humid environments (i.e.,
 369 $\overline{E_o}/\overline{P} \sim 1.0$). Despite a multitude of attempts over an extended period we were unable to develop a simple useful
 370 synthesis to summarise the partitioning of variability in those environments. We found that the three covariance
 371 terms all play important roles and we also found that simple environmental gradients (e.g., dry/wet, high/low
 372 storage capacity, hot/cold) could not easily explain the observed patterns. We anticipate that vegetation related
 373 processes (e.g., phenology, rooting depth, gas exchange characteristics, disturbance, etc.) may prove to be
 374 important in explaining hydrologic variability in these biologically productive regions that support most of human

375 population. This result implies that a major scientific effort will be needed to develop a synthesis of the controlling
376 factors for variability of the water cycle in these environments.

377

378 5. Discussion and Conclusions

379

380 Importantly, hydrologists have long been interested in hydrologic variability, but without readily available
381 databases it has been difficult to quantify water cycle variability. For example, we are not aware of maps showing
382 global spatial patterns in variance for any terms of the water balance (except for P). In this study, we describe an
383 initial investigation of the inter-annual variability of the terrestrial branch in the global water cycle that uses the
384 recently released global monthly Climate Data Record (CDR) database for P , E , Q and ΔS . The CDR is one of
385 the first dedicated hydrologic reanalysis databases and includes data for a 27-year period. Accordingly, we could
386 only examine hydrologic variability over this relatively short period. Further, we expect future improvements and
387 modifications as the hydrologic community seeks to further develop and refine these new reanalysis databases.
388 With those caveats in mind, we started this analysis by first investigating the partitioning of P in the water cycle
389 in terms of long-term mean and then extended that to the inter-annual variability using a theoretical variance
390 balance equation (Eq. 2). Despite the initial nature of this investigation we have been able to establish some useful
391 general principles.

392

393 The mean annual P is mostly partitioned into mean annual E and Q , as is well known, and the results using the
394 CDR were generally consistent with the earlier Budyko framework (Fig. 2). Having established that, the first
395 general finding is that the spatial pattern in the partitioning of inter-annual variability in the water cycle is not
396 simply a reflection of the spatial pattern in the partitioning of the long-term mean. In particular, with the variance
397 calculations, the annual anomalies are squared and hence the storage anomalies do not cancel out like they do
398 when calculating the mean. With that in mind, we were surprised that the inter-annual variability of water storage
399 change ($\sigma_{\Delta S}^2$) is typically larger than the inter-annual variability of evapotranspiration (σ_E^2) (cf. Fig. 3b and 3d).
400 The consequence is that $\sigma_{\Delta S}^2$ is more important than σ_E^2 for understanding inter-annual variability of global water
401 cycle. A second important generalisation is that unlike the variance components which are all positive, the three
402 covariance components in the theory (Eq. 2) can be both positive and negative. We report results here showing
403 both large positive and negative values for the three covariance terms (Fig. 3efg). This was especially prevalent
404 in biologically productive regions ($0.5 < \overline{E_o} / \overline{P} < 1.5$, Fig. 3eg). When examining the mean state, we are accustomed

405 to think that P sets a limit to E , Q and ΔS , as per the mass balance (Eq. 1). But the same thinking does not extend
406 to the variance balance since the covariance terms on the right hand side of Eq. 2 can be both large and negative
407 leading to circumstances where the variability in the sinks (σ_E^2 , σ_Q^2 , $\sigma_{\Delta S}^2$) could actually exceed variability in the
408 source (σ_P^2). These general principles of variance partitioning in the water cycle above may vary at different time
409 scales (e.g., monthly, daily), and we expect more details of the variability partitioning across various temporal
410 scales to be investigated in future studies.

411

412 Our initial attempt to develop deeper understanding of variance partitioning was based on a series of case studies
413 located in extreme environments (wet/dry vs hot/cold vs high/low water storage capacity). The results offered
414 some further insights about hydrologic variability. For example, under extremely dry (water-limited)
415 environments, with limited storage capacity (S_{\max}) we found that E follows P and σ_E^2 follows σ_P^2 , with σ_Q^2 and $\sigma_{\Delta S}^2$
416 both approaching zero. However, as S_{\max} increases, the partitioning of σ_P^2 progressively shifts to a balance between
417 σ_E^2 , $\sigma_{\Delta S}^2$ and $\text{cov}(E, \Delta S)$ (Figs. 10-12). This result explains the overestimation of σ_E/σ_P by the empirical theory of
418 Koster and Suarez (1999) which implicitly assumed no inter-annual change in storage. The Koster and Suarez
419 empirical theory is perhaps better described as an upper limit that is based on minimal storage capacity, and that
420 any increase in storage capacity would promote the partitioning of σ_P^2 to $\sigma_{\Delta S}^2$ particularly under dry conditions
421 (Figs. 10-12).

422

423 In extremely wet/hot environments (i.e., no snow/ice presence) we found σ_P^2 to be mostly partitioned to σ_Q^2 (with
424 both σ_E^2 and $\sigma_{\Delta S}^2$ approaching zero, Fig. 10). In contrast, in extremely wet/cold environments, the partitioning of
425 σ_P^2 was highly (spatially) variable presumably because of spatial variability in the all-important thermal processes
426 (freeze/melt).

427

428 The most complex results were found in mesic biologically productive environments ($0.5 < \overline{E_o}/\overline{P} < 1.5$), where all
429 three covariance terms (Eq. 2) were found to be relatively large and therefore they all played critical roles in the
430 overall partitioning of variability (Fig. 6). As noted above, in many of these regions, the (absolute) magnitudes of
431 the covariances were actually larger than the variances of the water balance components E , Q and ΔS (e.g., Fig.
432 3). That result demonstrates that deeper understanding of the process-level interactions that are embedded within

433 each of the three covariance terms (e.g., the role of seasonal vegetation variation) will be needed to develop
434 process-based understanding of variability in the water cycle in these biologically productive regions ($0.5 < \overline{E}_o / \overline{P} < 1.5$).
435

436

437 The syntheses of the long-term mean water cycle originated in 1970s (Budyko, 1974), and it took several decades
438 for those general principles to become widely adopted in the hydrologic community. The hydrologic data needed
439 to understand hydrologic variability are only now becoming available. With those data we can begin to develop a
440 process-based understanding of hydrologic variability that can be used for a variety of purposes, e.g., deeper
441 understanding of hydro-climatic behaviour, hydrologic risk analysis, climate change assessments and hydrologic
442 sensitivity studies are just a few applications that spring to mind. The initial results presented here show that a
443 major intellectual effort will be needed to develop a general understanding of hydrologic variability.

444

445 **Data availability**

446 The global terrestrial water budget used in this study can be accessed at
447 http://stream.princeton.edu:8080/pendap/MEaSURES/WC_MULTISOURCES_WB_050/ (Zhang et al., 2018).
448 The NASA/GEWEX Surface Radiation Budget (SRB) is available at
449 https://eosweb.larc.nasa.gov/project/srb/srb_table (Stackhouse et al., 2011). The global land air temperature
450 dataset from the Climatic Research Unit (CRU TS4.01 database) can be downloaded from
451 http://data.ceda.ac.uk/badc/cru/data/cru_ts/cru_ts_4.01 (Harris et al., 2014). The FLUXNET data is available at
452 <https://fluxnet.fluxdata.org/>. The LandFluxEval, MPI and E-RUN databases used for further validation are
453 published by Mueller et al. (2013), Jung et al. (2010) and Gudmundsson and Seneviratne (2016), respectively.

454

455 **Author contributions**

456 D. Yin and M. L. Roderick designed the study and are both responsible for the integrity of the manuscript. D. Yin
457 performed the calculations and analyses, and prepared the original manuscript, and M. L. Roderick contributed to
458 the interpretation, discussion and writing of the manuscript.

459

460 **Competing interests**

461 The authors declare that they have no conflict of interest.

462

463 **Acknowledgements**

464 This research was supported by the Australian Research Council (CE11E0098, CE170100023), and D.Y. also
465 acknowledges support by the National Natural Science Foundation of China (51609122). We thank Dr Anna
466 Ukkola for help in accessing the FLUXNET database. We thank the reviewers (including Dr René Orth and two
467 anonymous reviewers) for helpful comments that improved the manuscript.

468

469 **References**

470 Agarwal, D. A., Humphrey, M., Beekwilder, N. F., Jackson, K. R., Goode, M. M., and van Ingen, C.: A data-centered
471 collaboration portal to support global carbon-flux analysis, *Concurr. Comp-Pract. E.*, 22, 2323-2334,
472 <https://doi.org/10.1002/cpe.1600>, 2010.

473 Baldocchi, D., Falge, E., Gu, L., Olson, R., Hollinger, D., Running, S., Anthoni, P., Bernhofer, C., Davis, K., Evans, R.,
474 Fuentes, J., Goldstein, A., Katul, G., Law, B., Lee, X., Malhi, Y., Meyers, T., Munger, W., Oechel, W., Paw U, K. T.,
475 Pilegaard, K., Schmid, H. P., Valentini, R., Verma, S., Vesala, T., Wilson, K., and Wofsy, S.: FLUXNET: A New Tool
476 to Study the Temporal and Spatial Variability of Ecosystem-Scale Carbon Dioxide, Water Vapor, and Energy Flux
477 Densities, *B. Am. Meteorol. Soc.*, 82, 2415-2434, [https://doi.org/10.1175/1520-
478 0477\(2001\)082<2415:FANTTS>2.3.CO;2](https://doi.org/10.1175/1520-0477(2001)082<2415:FANTTS>2.3.CO;2), 2001.

479 Balsamo, G., Albergel, C., Beljaars, A., Boussetta, S., Brun, E., Cloke, H., Dee, D., Dutra, E., Muñoz-Sabater, J.,
480 Pappenberger, F., de Rosnay, P., Stockdale, T., and Vitart, F.: ERA-Interim/Land: a global land surface reanalysis
481 data set, *Hydrol. Earth Syst. Sci.*, 19, 389-407, 10.5194/hess-19-389-2015, 2015.

482 Budyko, M. I.: *Climate and Life*. Academic Press, London, 1974.

483 Choudhury, B. J.: Evaluation of an empirical equation for annual evaporation using field observations and results
484 from a biophysical model, *J. Hydrol.*, 216, 99-110, [https://doi.org/10.1016/S0022-1694\(98\)00293-5](https://doi.org/10.1016/S0022-1694(98)00293-5), 1999.

485 Dee, D. P., Uppala, S. M., Simmons, A. J., Berrisford, P., Poli, P., Kobayashi, S., Andrae, U., Balmaseda, M. A.,
486 Balsamo, G., Bauer, P., Bechtold, P., Beljaars, A. C. M., van de Berg, L., Bidlot, J., Bormann, N., Delsol, C., Dragani,
487 R., Fuentes, M., Geer, A. J., Haimberger, L., Healy, S. B., Hersbach, H., Hólm, E. V., Isaksen, L., Kållberg, P., Köhler,
488 M., Matricardi, M., McNally, A. P., Monge-Sanz, B. M., Morcrette, J. J., Park, B. K., Peubey, C., de Rosnay, P.,
489 Tavolato, C., Thépaut, J. N., and Vitart, F.: The ERA-Interim reanalysis: configuration and performance of the
490 data assimilation system, *Q. J. R. Meteorol. Soc.*, 137, 553-597, <https://doi.org/10.1002/qj.828>, 2011.

491 Donohue, R. J., Roderick, M. L., and McVicar, T. R.: Can dynamic vegetation information improve the accuracy of
492 Budyko's hydrological model?, *J. Hydrol.*, 390, 23-34, <https://doi.org/10.1016/j.jhydrol.2010.06.025>, 2010.

493 Fu, B. P.: On the Calculation of the Evaporation from Land Surface, *Sci. Atmos. Sin.*, 5, 23-31, 1981.

494 Gudmundsson, L., Greve, P., and Seneviratne, S. I.: The sensitivity of water availability to changes in the aridity
495 index and other factors—A probabilistic analysis in the Budyko space, *Geophys. Res. Lett.*, 43, 6985-6994,
496 <https://doi.org/10.1002/2016GL069763>, 2016.

497 Gudmundsson, L., and Seneviratne, S. I.: Observation-based gridded runoff estimates for Europe (E-RUN version
498 1.1), *Earth Syst. Sci. Data*, 8, 279-295, 10.5194/essd-8-279-2016, 2016.

499 Harris, I., Jones, P. D., Osborn, T. J., and Lister, D. H.: Updated high-resolution grids of monthly climatic
500 observations—the CRU TS3.10 Dataset, *Int. J. Climatol.*, 34, 623-642, <https://doi.org/10.1002/joc.3711>, 2014.

501 Huning, L. S., and AghaKouchak, A.: Mountain snowpack response to different levels of warming, *Proc. Natl.
502 Acad. Sci. U. S. A.*, 115, 10932, <https://doi.org/10.1073/pnas.1805953115>, 2018.

503 Jackson, R. B., Canadell, J., Ehleringer, J. R., Mooney, H. A., Sala, O. E., and Schulze, E. D.: A Global Analysis of
504 Root Distributions for Terrestrial Biomes, *Oecologia*, 108, 389-411, <https://doi.org/10.1007/BF00333714>, 1996.

505 Jung, M., Reichstein, M., Ciais, P., Seneviratne, S. I., Sheffield, J., Goulden, M. L., Bonan, G., Cescatti, A., Chen, J.,
506 de Jeu, R., Dolman, A. J., Eugster, W., Gerten, D., Gianelle, D., Gobron, N., Heinke, J., Kimball, J., Law, B. E.,
507 Montagnani, L., Mu, Q., Mueller, B., Oleson, K., Papale, D., Richardson, A. D., Rouspard, O., Running, S., Tomelleri,
508 E., Viovy, N., Weber, U., Williams, C., Wood, E., Zaehle, S., and Zhang, K.: Recent decline in the global land
509 evapotranspiration trend due to limited moisture supply, *Nature*, 467, 951,
510 <https://doi.org/10.1038/nature09396>, 2010.

511 Koster, R. D., and Suarez, M. J.: A Simple Framework for Examining the Interannual Variability of Land Surface
512 Moisture Fluxes, *J. Clim.*, 12, 1911-1917, [https://doi.org/10.1175/1520-0442\(1999\)012<1911:ASFFET>2.0.CO;2](https://doi.org/10.1175/1520-0442(1999)012<1911:ASFFET>2.0.CO;2),
513 1999.

514 McMahon, T. A., Peel, M. C., Pegram, G. G. S., and Smith, I. N.: A Simple Methodology for Estimating Mean and
515 Variability of Annual Runoff and Reservoir Yield under Present and Future Climates, *J. Hydrometeorol.*, 12, 135-
516 146, <https://doi.org/10.1175/2010jhm1288.1>, 2011.

517 Milly, P. C. D.: Climate, soil water storage, and the average annual water balance, *Water Resour. Res.*, 30, 2143-
518 2156, <https://doi.org/10.1029/94WR00586>, 1994a.

519 Milly, P. C. D.: Climate, interseasonal storage of soil water, and the annual water balance, *Adv. Water Resour.*,
520 17, 19-24, [https://doi.org/10.1016/0309-1708\(94\)90020-5](https://doi.org/10.1016/0309-1708(94)90020-5), 1994b.

521 Milly, P. C. D., and Dunne, K. A.: Macroscale water fluxes 1. Quantifying errors in the estimation of basin mean
522 precipitation, *Water Resour. Res.*, 38, 23-21-23-14, <https://doi.org/10.1029/2001WR000759>, 2002a.

523 Milly, P. C. D., and Dunne, K. A.: Macroscale water fluxes 2. Water and energy supply control of their interannual
524 variability, *Water Resour. Res.*, 38, 24-21-24-29, <https://doi.org/10.1029/2001WR000760>, 2002b.

525 Mueller, B., Hirschi, M., Jimenez, C., Ciais, P., Dirmeyer, P. A., Dolman, A. J., Fisher, J. B., Jung, M., Ludwig, F.,
526 Maignan, F., Miralles, D. G., McCabe, M. F., Reichstein, M., Sheffield, J., Wang, K., Wood, E. F., Zhang, Y., and
527 Seneviratne, S. I.: Benchmark products for land evapotranspiration: LandFlux-EVAL multi-data set synthesis,
528 *Hydrol. Earth. Syst. Sci.*, 17, 3707-3720, <https://doi.org/10.5194/hess-17-3707-2013>, 2013.

529 Norby, R. J., Ledford, J., Reilly, C. D., Miller, N. E., and O'Neill, E. G.: Fine-root production dominates response of
530 a deciduous forest to atmospheric CO₂ enrichment, *Proc. Natl. Acad. Sci. U. S. A.*, 101, 9689-9693,
531 <https://doi.org/10.1073/pnas.0403491101>, 2004.

532 Orth, R., and Destouni, G.: Drought reduces blue-water fluxes more strongly than green-water fluxes in Europe,
533 *Nat. Commun.*, 9, 3602, <https://doi.org/10.1038/s41467-018-06013-7>, 2018.

534 Padrón, R. S., Gudmundsson, L., Greve, P., and Seneviratne, S. I.: Large-Scale Controls of the Surface Water
535 Balance Over Land: Insights From a Systematic Review and Meta-Analysis, *Water Resources Research*, 53, 9659-
536 9678, 10.1002/2017WR021215, 2017.

537 Reichle, R. H., Koster, R. D., De Lannoy, G. J. M., Forman, B. A., Liu, Q., Mahanama, S. P. P., and Touré, A.:
538 Assessment and Enhancement of MERRA Land Surface Hydrology Estimates, *Journal of Climate*, 24, 6322-6338,
539 10.1175/JCLI-D-10-05033.1, 2011.

540 Rodell, M., Beaudoin, H. K., L'Ecuyer, T. S., Olson, W. S., Famiglietti, J. S., Houser, P. R., Adler, R., Bosilovich, M.
541 G., Clayson, C. A., Chambers, D., Clark, E., Fetzer, E. J., Gao, X., Gu, G., Hilburn, K., Huffman, G. J., Lettenmaier,
542 D. P., Liu, W. T., Robertson, F. R., Schlosser, C. A., Sheffield, J., and Wood, E. F.: The Observed State of the Water
543 Cycle in the Early Twenty-First Century, *J. Clim.*, 28, 8289-8318, <https://doi.org/10.1175/JCLI-D-14-00555.1>,
544 2015.

545 Roderick, M. L., and Farquhar, G. D.: A simple framework for relating variations in runoff to variations in climatic
546 conditions and catchment properties, *Water Resour. Res.*, 47, <https://doi.org/10.1029/2010WR009826>, 2011.

547 Sankarasubramanian, A., and Vogel, R. M.: Annual hydroclimatology of the United States, *Water Resour. Res.*,
548 38, 19-11-19-12, <https://doi.org/10.1029/2001WR000619>, 2002.

549 Scanlon, B. R., Zhang, Z., Save, H., Sun, A. Y., Müller Schmied, H., van Beek, L. P. H., Wiese, D. N., Wada, Y., Long,
550 D., Reedy, R. C., Longuevergne, L., Döll, P., and Bierkens, M. F. P.: Global models underestimate large decadal
551 declining and rising water storage trends relative to GRACE satellite data, *Proc. Natl. Acad. Sci. U. S. A.*,
552 <https://doi.org/10.1073/pnas.1704665115>, 2018.

553 Sposito, G.: Understanding the Budyko Equation, *Water*, 9, <https://doi.org/10.3390/w9040236>, 2017.

554 Stackhouse, P. W., Gupta, S. K., Cox, S. J., Mikovitz, J. C., Zhang, T., and Hinkelman, L. M.: The NASA/GEWEX
555 Surface Radiation Budget Release 3.0: 24.5-Year Dataset. In: *GEWEX News*, No. 1, 2011.

556 Ukkola, A. M., Haughton, N., De Kauwe, M. G., Abramowitz, G., and Pitman, A. J.: FluxnetLSM R package (v1.0):
557 a community tool for processing FLUXNET data for use in land surface modelling, *Geosci. Model. Dev.*, 10, 3379-
558 3390, <https://doi.org/10.5194/gmd-10-3379-2017>, 2017.

559 Wang, D., and Alimohammadi, N.: Responses of annual runoff, evaporation, and storage change to climate
560 variability at the watershed scale, *Water Resour. Res.*, 48, <https://doi.org/10.1029/2011WR011444>, 2012.

561 Wang-Erlandsson, L., Bastiaanssen, W. G. M., Gao, H., Jägermeyr, J., Senay, G. B., van Dijk, A. I. J. M., Guerschman,
562 J. P., Keys, P. W., Gordon, L. J., and Savenije, H. H. G.: Global root zone storage capacity from satellite-based
563 evaporation, *Hydrol. Earth Syst. Sci.*, 20, 1459-1481, <https://doi.org/10.5194/hess-2015-533>, 2016.

564 Yang, H., Yang, D., Lei, Z., and Sun, F.: New analytical derivation of the mean annual water-energy balance
565 equation, *Water Resour. Res.*, 44, <https://doi.org/10.1029/2007WR006135>, 2008.

566 Yang, Y., Donohue, R. J., and McVicar, T. R.: Global estimation of effective plant rooting depth: Implications for
567 hydrological modeling, *Water Resour. Res.*, 52, 8260-8276, <https://doi.org/10.1002/2016WR019392>, 2016.

568 Zeng, R., and Cai, X.: Assessing the temporal variance of evapotranspiration considering climate and catchment
569 storage factors, *Adv. Water Resour.*, 79, 51-60, <https://doi.org/10.1016/j.advwatres.2015.02.008>, 2015.

570 Zhang, L., Potter, N., Hickel, K., Zhang, Y., and Shao, Q.: Water balance modeling over variable time scales based
571 on the Budyko framework – Model development and testing, *J. Hydrol.*, 360, 117-131,
572 <https://doi.org/10.1016/j.jhydrol.2008.07.021>, 2008.

573 Zhang, Y., Pan, M., Sheffield, J., Siemann, A. L., Fisher, C. K., Liang, M. L., Beck, H. E., Wanders, N., MacCracken,
574 R. F., Houser, P. R., Zhou, T., Lettenmaier, D. P., Ma, Y., Pinker, R. T., Bytheway, J., Kummerow, C. D., and Wood,

575 E. F.: A Climate Data Record (CDR) for the global terrestrial water budget: 1984-2010, Hydrol. Earth Syst. Sci., 22,
576 241-263, <https://doi.org/10.5194/hess-22-241-2018>, 2018.

577

578

579 **List of Figures:**

580 Figure 1. Mean annual (1984-2010) (a) P , (b) E and (c) Q . Note that the mean annual ΔS in the CDR database is
581 zero by construction and is not shown.

582 Figure 2. Relationship of mean annual (a) evapotranspiration (\bar{E}/\bar{P}) and (b) runoff (\bar{Q}/\bar{P}) ratios to the aridity
583 index (\bar{E}_o/\bar{P}) from the CDR and SRB databases. For comparison, the Budyko (1974) curve is shown on the left
584 panel (Fig. 2a). The curve on the right panel (Fig. 2b) is calculated assuming a steady state ($\bar{Q}/\bar{P} = 1 - \bar{E}/\bar{P}$).

585 Figure 3. Water cycle variances ($\sigma_P^2, \sigma_E^2, \sigma_Q^2, \sigma_{\Delta S}^2$) and covariances ($cov(E, Q), cov(E, \Delta S), cov(Q, \Delta S)$). Note
586 that we have multiplied the covariances by two (see Eq. 2).

587 Figure 4. Relation between inter-annual mean and standard deviation for (a) P , (b) E and (c) Q from the CDR
588 database. Note that the mean annual ΔS is zero by construction and is not shown.

589 Figure 5. Relationship of inter-annual standard deviation of (a) evapotranspiration (σ_E/σ_P) and (b) runoff (σ_Q/σ_P)
590 ratios to aridity (\bar{E}_o/\bar{P}). The curves represent the semi-empirical relations from Koster and Suarez (1999).

591 Figure 6. Relation between water cycle variances-covariances (see Fig. 3b-g) as a fraction of the variance of P
592 (σ_P^2) and the aridity index (\bar{E}_o/\bar{P}) coloured by density. Note that we have multiplied the covariance components
593 by two (see Eq. 2).

594 Figure 7. Relation between water cycle variances-covariances (see Fig. 3b-g) as a fraction of the variance for P
595 (σ_P^2) and the aridity index (\bar{E}_o/\bar{P}) for grid-cells over different latitude ranges (i.e., 90N-60N, 60N-30N, 30N-0
596 and 0-90S). The colours relate to the water storage capacity S_{\max} . Note that we have multiplied the covariances by
597 two (see Eq. 2). The vertical grey dashed lines represent thresholds used to separate extremely dry ($\bar{E}_o/\bar{P} \geq 6.0$)
598 and wet ($\bar{E}_o/\bar{P} \leq 0.5$) environments. Note the use of a logarithmic x-axis and scale bar for S_{\max} .

599 Figure 8. Relation between water cycle variances-covariances (see Fig. 3b-g) as a fraction of the variance for P
600 (σ_P^2) and the aridity index (\bar{E}_o/\bar{P}) for grid-cells over different latitude ranges (i.e., 90N-60N, 60N-30N, 30N-0
601 and 0-90S). The colours relate to the mean air temperature (\bar{T}_a). Note that we have multiplied the covariances by
602 two (see Eq. 2). The vertical grey dashed lines represent thresholds used to separate extremely dry ($\bar{E}_o/\bar{P} \geq 6.0$)
603 and wet ($\bar{E}_o/\bar{P} \leq 0.5$) environments.

604 Figure 9. Locations of three representative grid-cells used as case study sites.

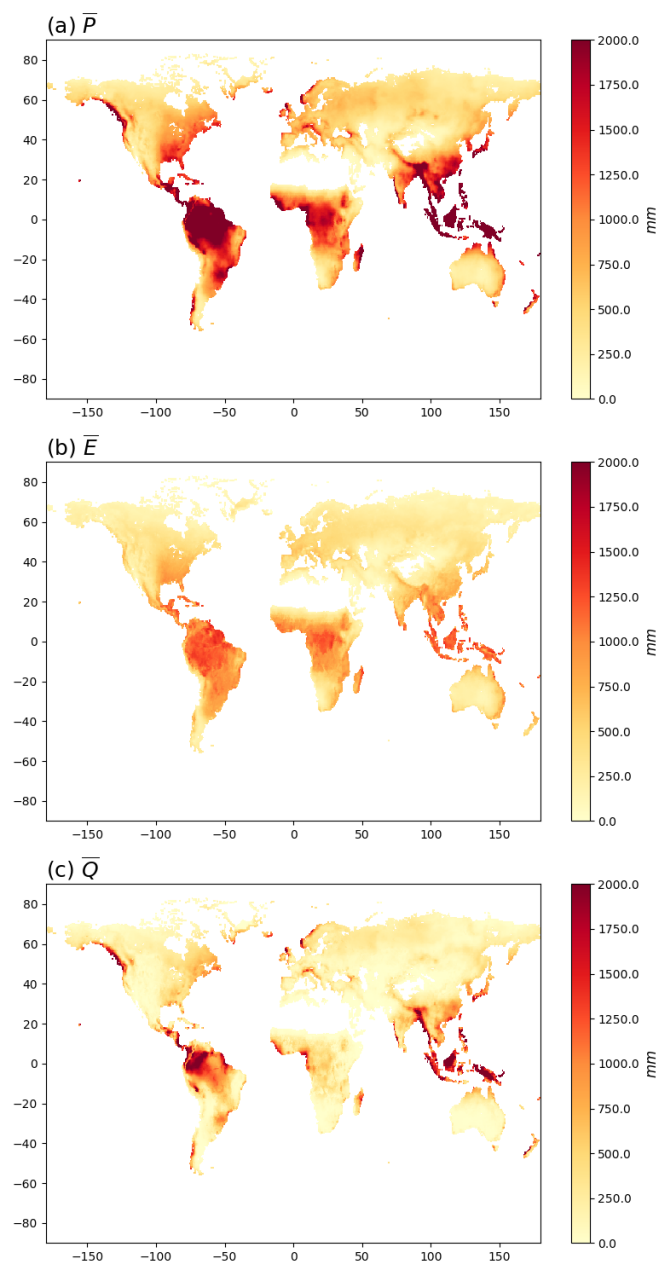
605 Figure 10. Inter-annual time series (P, E, Q and ΔS) and the associated variance-covariance matrix (E, Q and ΔS)
606 for case study Sites 1-3. Left column shows time series for (a) Site 1, (c) Site 2 and (e) Site 3, with right column
607 i.e., (b), (d) and (f), the associated variance-covariance matrix for three sites. Note that the covariance values in
608 the tables should be multiplied by two to agree with the variance-covariance balance in Eq. (2).

609 Figure 11. Location of three case study sites in the water cycle variability space. The grey background dots are
610 from Fig. 6.

611 Figure 12. Synthesis of factors controlling variance partitioning. The arrows denote trends with increasing S_{\max} .
612 The grey background dots are from Fig. 6.

613

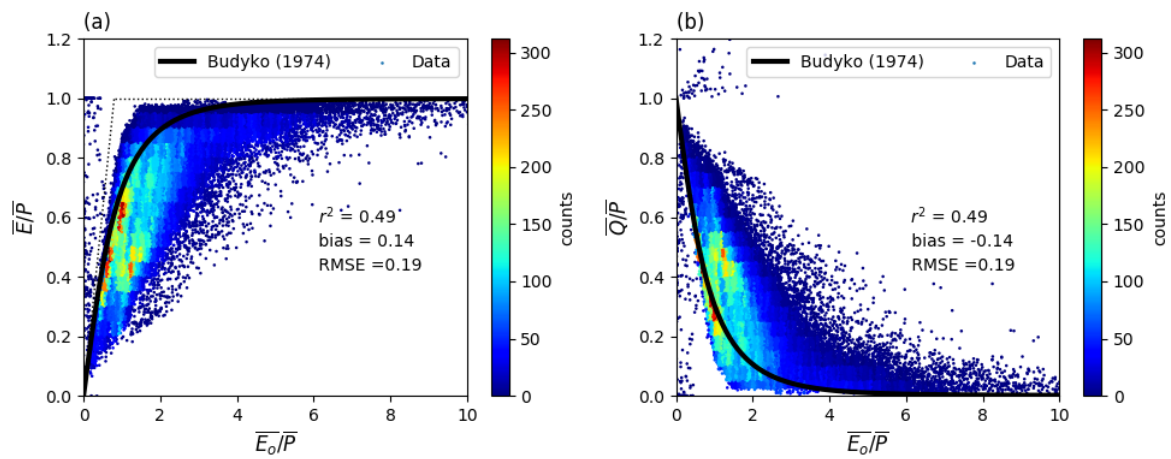
614
615



616
617
618
619

Figure 1. Mean annual (1984-2010) (a) P , (b) E and (c) Q . Note that the mean annual ΔS in the CDR database is zero by construction and is not shown.

620



621

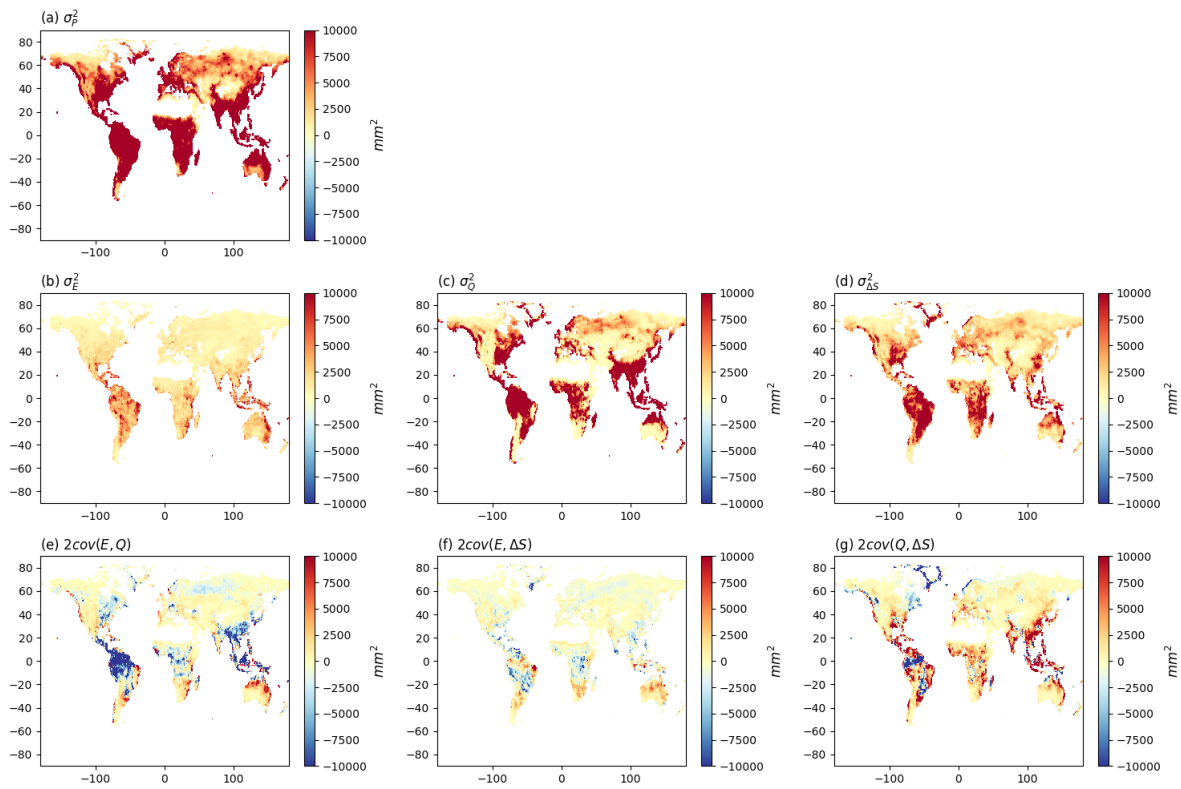
622 **Figure 2. Relationship of mean annual (a) evapotranspiration (\bar{E}/\bar{P}) and (b) runoff (\bar{Q}/\bar{P}) ratios to the aridity index**

623 **(\bar{E}_o/\bar{P}) from the CDR and SRB databases. For comparison, the Budyko (1974) curve is shown on the left panel (Fig.**

624 **2a). The curve on the right panel (Fig. 2b) is calculated assuming a steady state ($\bar{Q}/\bar{P} = 1 - \bar{E}/\bar{P}$).**

625

626

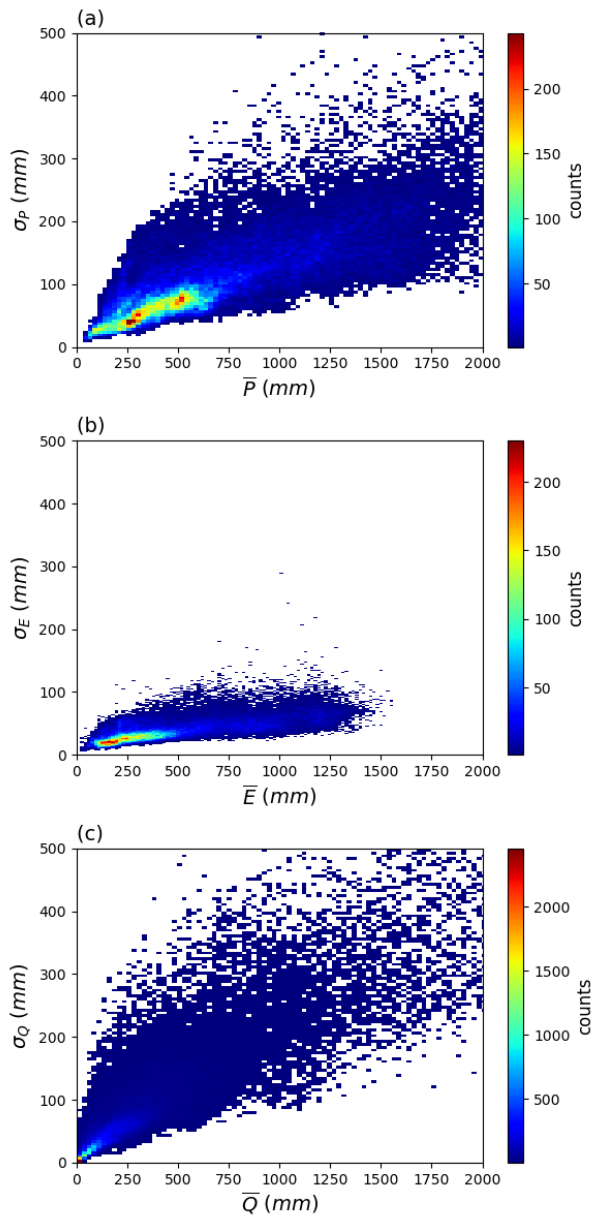


627

628 **Figure 3. Water cycle variances (σ_p^2 , σ_E^2 , σ_Q^2 , $\sigma_{\Delta S}^2$) and covariances ($cov(E, Q)$, $cov(E, \Delta S)$, $cov(Q, \Delta S)$). Note that we**
629 **have multiplied the covariances by two (see Eq. 2).**

630

631
632



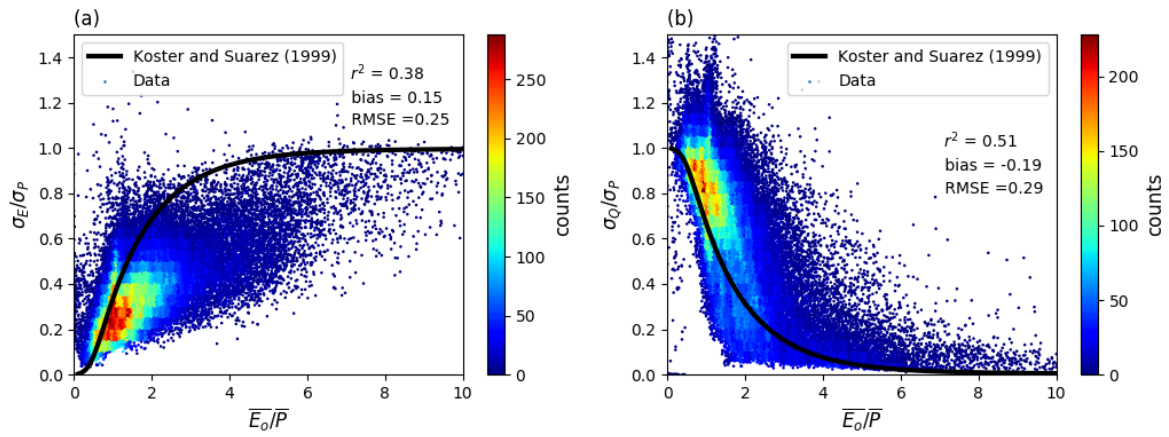
633

634 **Figure 4. Relation between inter-annual mean and standard deviation for (a) P , (b) E and (c) Q from the CDR**

635 **database. Note that the mean annual ΔS is zero by construction and is not shown.**

636

637



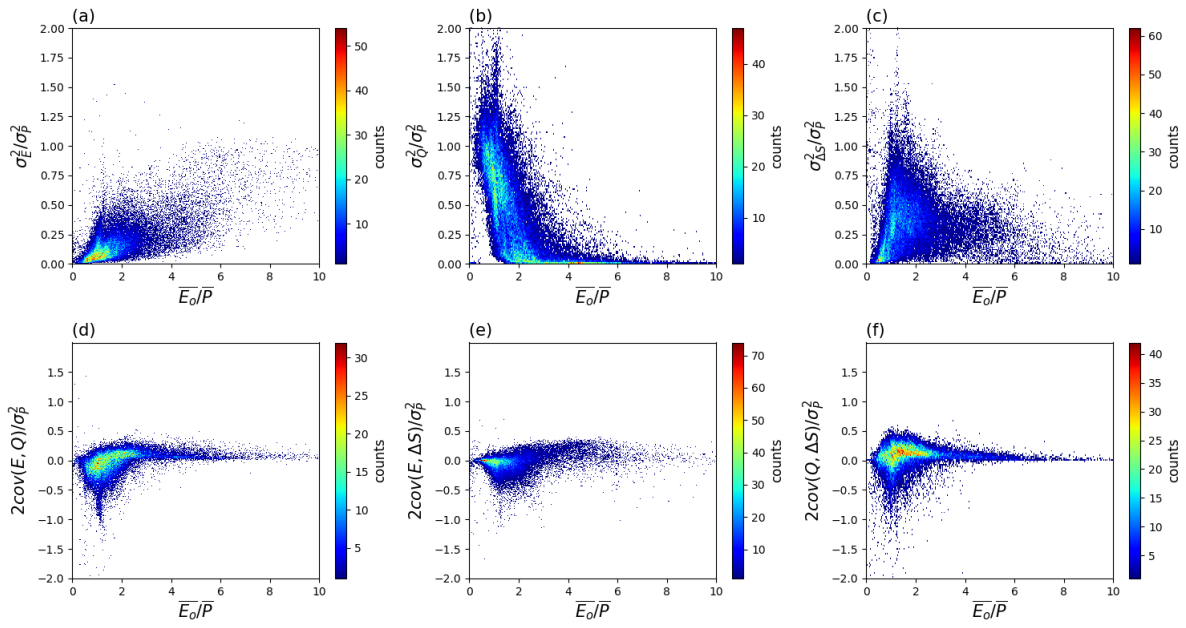
638

639 **Figure 5. Relationship of inter-annual standard deviation of (a) evapotranspiration (σ_E/σ_P) and (b) runoff (σ_Q/σ_P)**

640 **ratios to aridity (\bar{E}_o/\bar{P}). The curves represent the semi-empirical relations from Koster and Suarez (1999).**

641

642



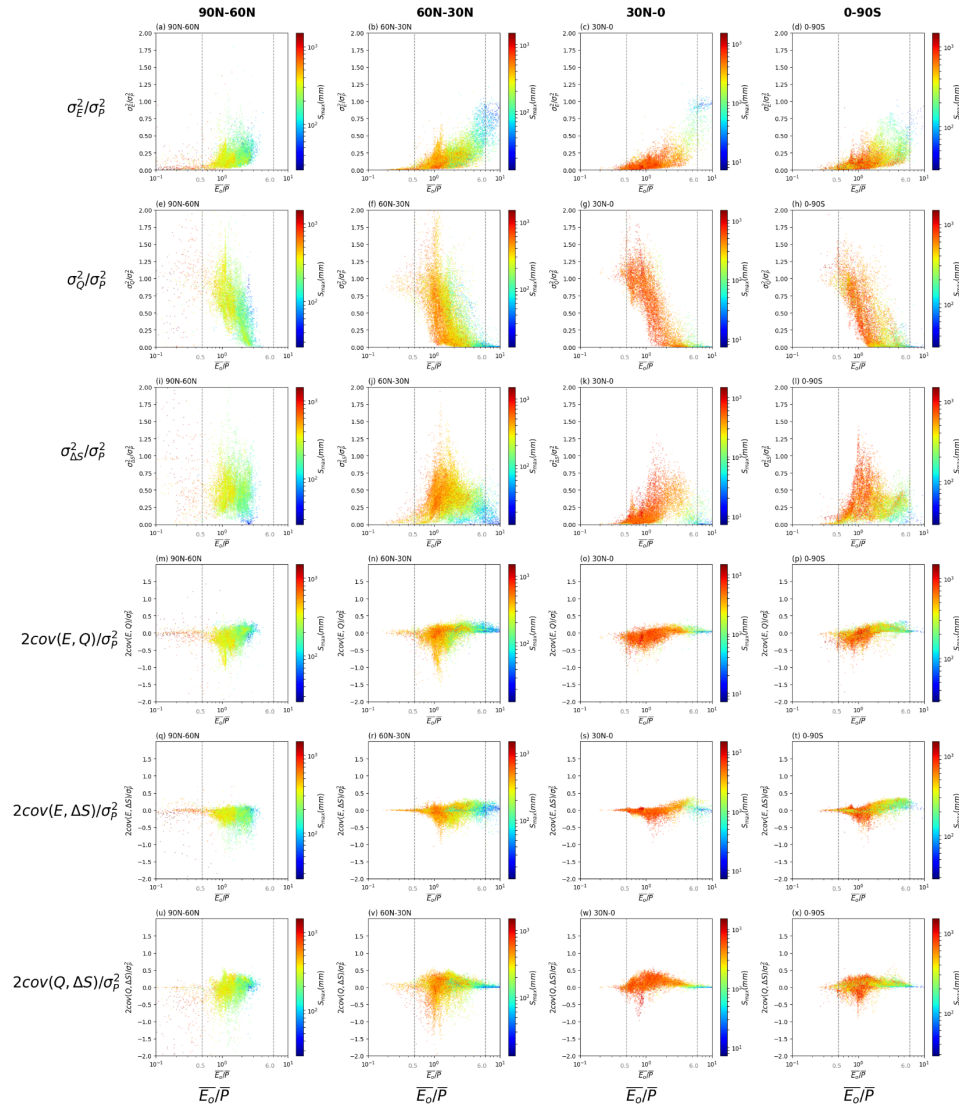
643

644 **Figure 6. Relation between water cycle variances-covariances (see Fig. 3b-g) as a fraction of the variance of P (σ_P^2) and**

645 **the aridity index (\bar{E}_o/\bar{P}) coloured by density. Note that we have multiplied the covariance components by two (see Eq.**

646 **2).**

647



649

650 **Figure 7.** Relation between water cycle variances-covariances (see Fig. 3b-g) as a fraction of the variance for P (σ_P^2)

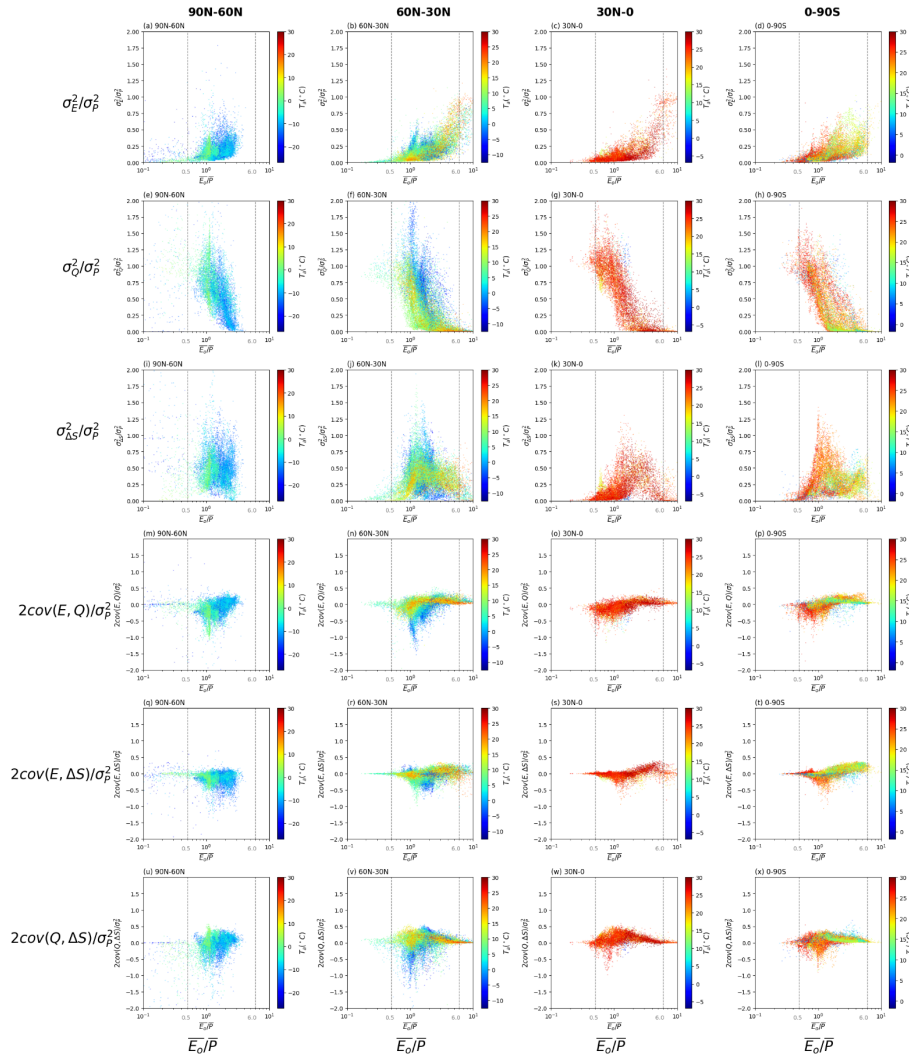
651 and the aridity index ($\overline{E_0}/\overline{P}$) for grid-cells over different latitude ranges (i.e., 90N-60N, 60N-30N, 30N-0 and 0-90S).

652 The colours relate to the water storage capacity S_{\max} . Note that we have multiplied the covariances by two (see Eq. 2).

653 The vertical grey dashed lines represent thresholds used to separate extremely dry ($\overline{E_0}/\overline{P} \geq 6.0$) and wet ($\overline{E_0}/\overline{P} \leq 0.5$)

654 environments. Note the use of a logarithmic x-axis and scale bar for S_{\max} .

655



657

658

659

660

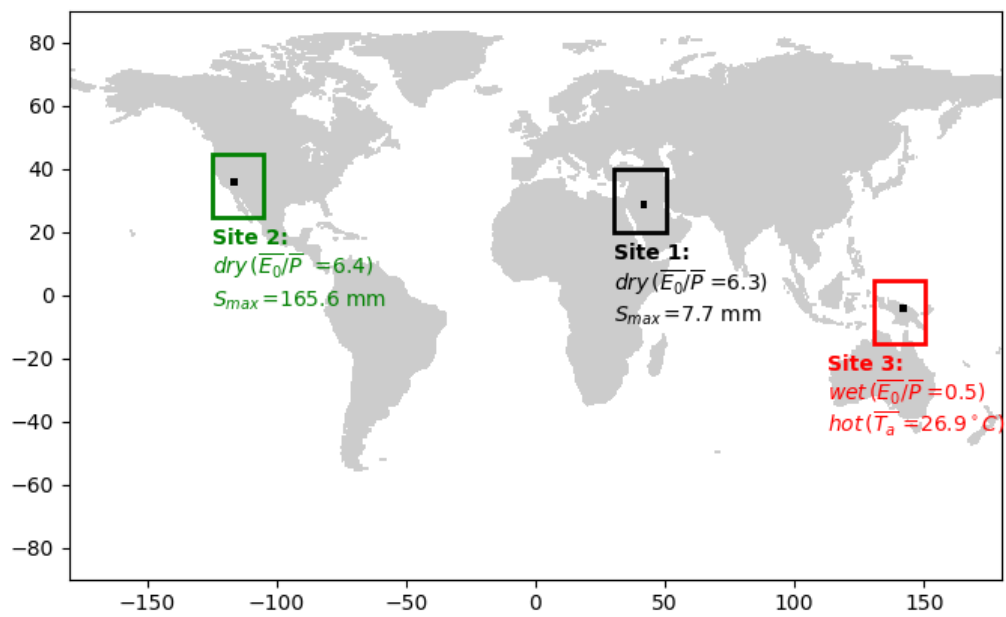
661

662

663

Figure 8. Relation between water cycle variances-covariances (see Fig. 3b-g) as a fraction of the variance for P (σ_P^2) and the aridity index ($\overline{E}_0/\overline{P}$) for grid-cells over different latitude ranges (i.e., 90N-60N, 60N-30N, 30N-0 and 0-90S). The colours relate to the mean air temperature (\overline{T}_a). Note that we have multiplied the covariances by two (see Eq. 2). The vertical grey dashed lines represent thresholds used to separate extremely dry ($\overline{E}_0/\overline{P} \geq 6.0$) and wet ($\overline{E}_0/\overline{P} \leq 0.5$) environments.

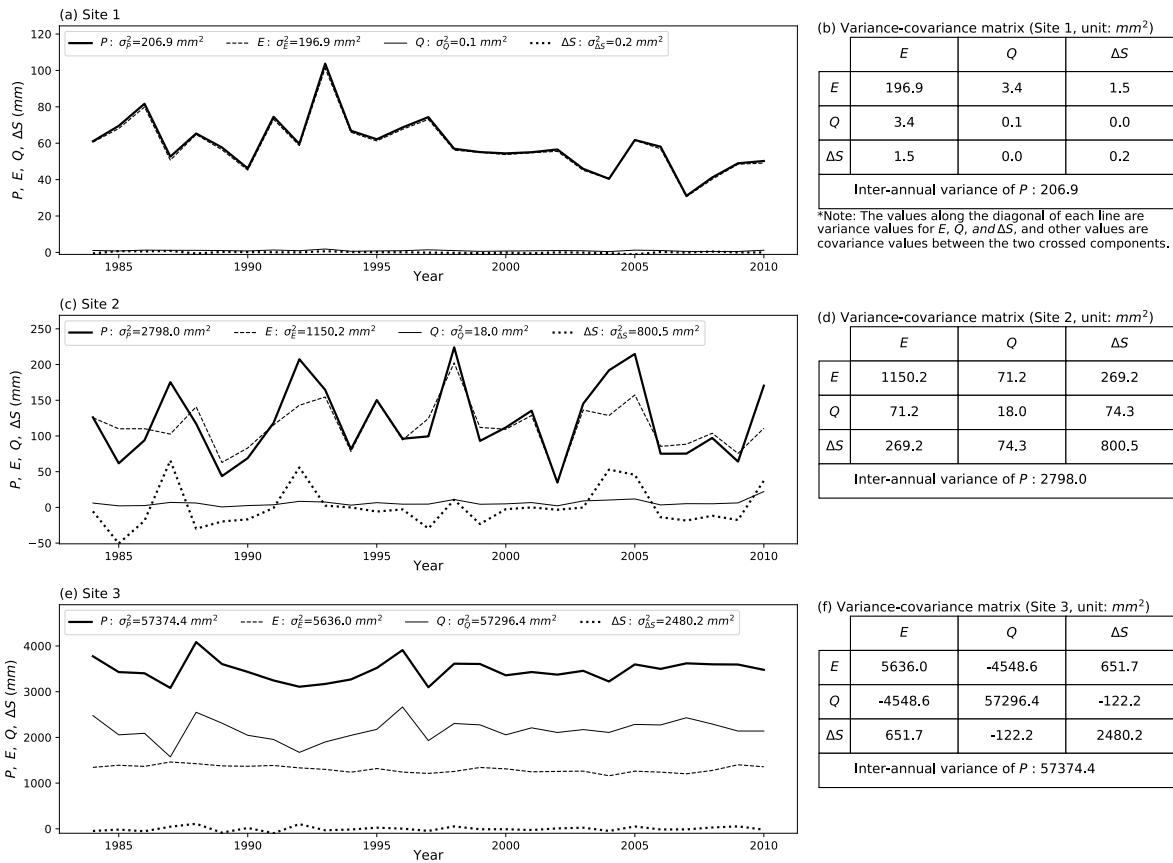
664



665

666 Figure 9. Locations of three representative grid-cells used as case study sites.

667

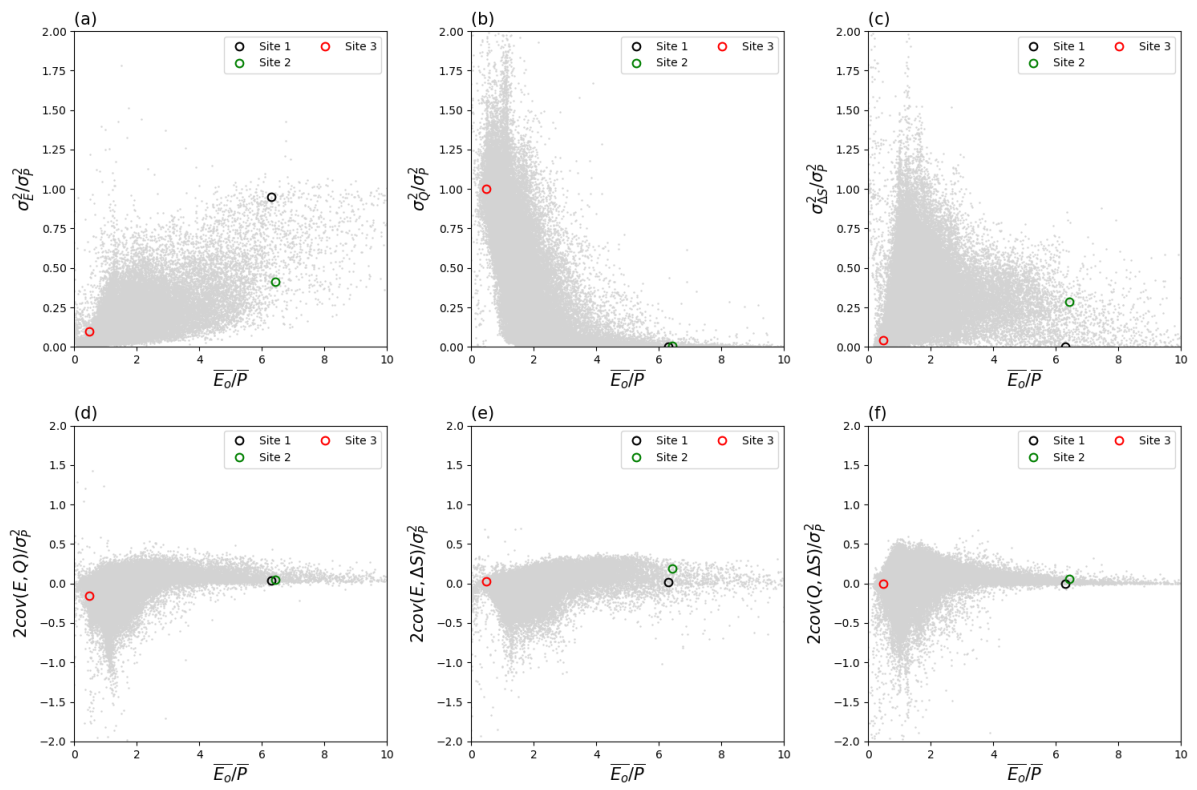


669

670 **Figure 10. Inter-annual time series (P , E , Q and ΔS) and the associated variance-covariance matrix (E , Q and ΔS) for**
 671 **case study Sites 1-3. Left column shows time series for (a) Site 1, (c) Site 2 and (e) Site 3, with right column i.e., (b), (d)**
 672 **and (f), the associated variance-covariance matrix for three sites. Note that the covariance values in the tables should**
 673 **be multiplied by two to agree with the variance-covariance balance in Eq. (2).**

674

675



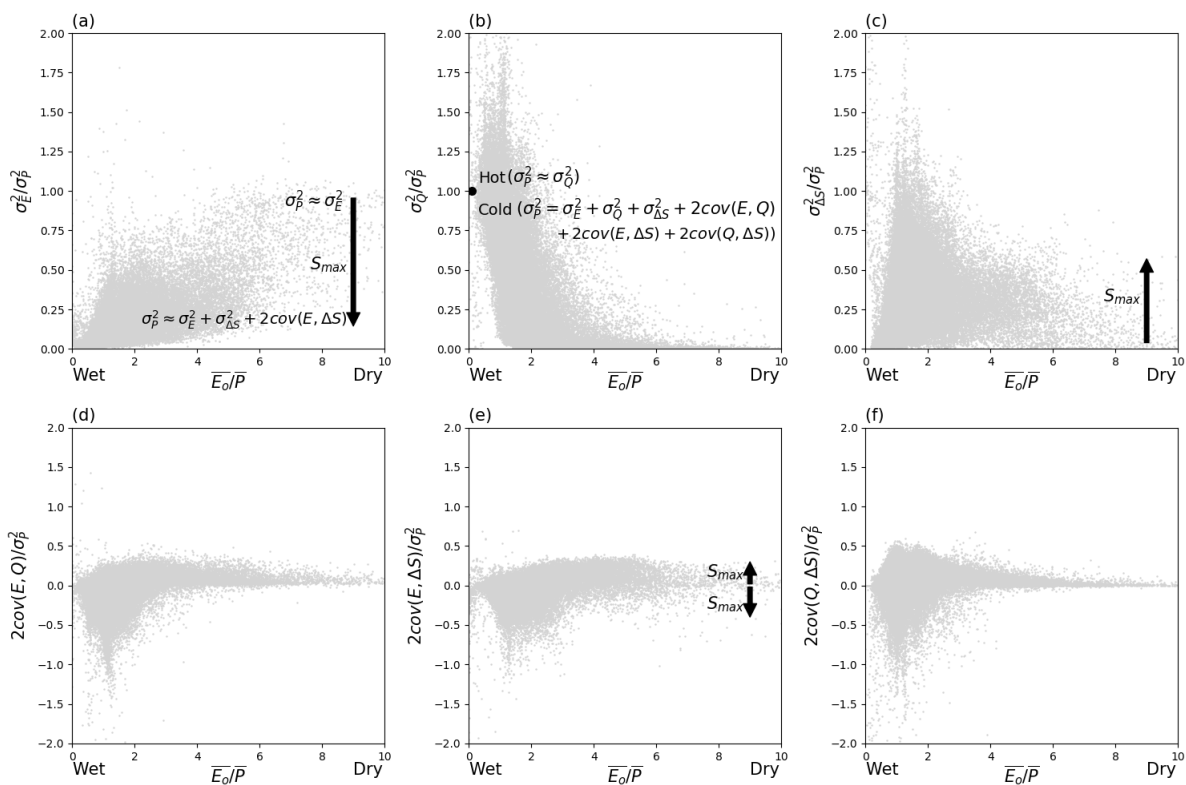
676

677 **Figure 11. Location of three case study sites in the water cycle variability space. The grey background dots are from**

678 **Fig. 6.**

679

680



681

682 **Figure 12. Synthesis of factors controlling variance partitioning. The arrows denote trends with increasing S_{max} . The**

683 **grey background dots are from Fig. 6.**

684